



Little Ice Age flood events recorded in sag pond sediments in the Carrizo Plains National Monument, California

Matthew Kirby · Samuel K. Hippard ·
Lisa N. Martinez · Dahlia Serrato · Joseph Carlin ·
Nicole Bonuso · Sinan O. Akçiz · Christian Novich

Received: 26 September 2023 / Accepted: 24 January 2024
© The Author(s), under exclusive licence to Springer Nature B.V. 2024

Abstract In California, severe precipitation events (SPEs) are often associated with winter season atmospheric rivers. These SPEs can generate hurricane-scale precipitation, creating a variety of natural hazards such as floods and landslides. For California, the most complete SPE-flood record yet generated is a 9000-year paleoflood reconstruction from the Santa Barbara Basin (Du et al. in Mar Geol 397:29–42,

2018). Finding terrestrial counterparts to compare to the Santa Barbara Basin is a challenge in Southern California where lake basins are rare and the terrestrial spatiotemporal signature of SPE floods remains largely unconstrained. Here, we present five 1–2 m sediment cores from a sag pond along the San Andreas Fault in the southern Carrizo Plain. The most complete record (core CLPC21-4) was selected for a variety of chronological, sedimentological, and biological analyses. Principal Component Analysis on these data reveals two end member sediment unit types: *event* versus *ambient* sedimentation. We focus on the two thickest sediment units likely generated by SPEs. These two units (EU 1 and EU 2) are especially distinct within CLPC21-4, characterized by erosive bases, above average sand content, normal grading, low magnetic susceptibility, and low total organic matter. Moreover, they are visually apparent across all five cores within the sag pond and thin from source to sink. Age control for the two units is constrained by AMS ^{14}C dates on discrete organic materials and supported by the identification of *Erodium*'s first appearance ca. 1750–1765 CE in the Santa Barbara region. Using these age constraints, we infer the maximum limiting age range for Event Unit 1 from 1470 to 1640 CE and Event Unit 2 from 1740 to 1800 CE. Within the limits of dating, site-specific proxy sensitivities, and inherent meteorological heterogeneity, we propose a probable correlation to Santa Barbara Basin flood events at 1525 CE and 1760 CE. Our results suggest that sag ponds may represent a viable

Supplementary Information The online version contains supplementary material available at <https://doi.org/10.1007/s10933-024-00312-4>.

M. Kirby (✉) · S. K. Hippard · D. Serrato · J. Carlin ·
N. Bonuso · S. O. Akçiz · C. Novich
Department of Geological Sciences, California State
University, Fullerton, Fullerton, CA 92834, USA
e-mail: mkirby@fullerton.edu

S. K. Hippard
e-mail: hippardsam@csu.fullerton.edu

D. Serrato
e-mail: dserrato@Fullerton.edu

J. Carlin
e-mail: jcarlin@fullerton.edu

S. O. Akçiz
e-mail: sakciz@fullerton.edu

C. Novich
e-mail: novichc@csu.fullerton.edu

L. N. Martinez
Department of Geography, University of California, Los
Angeles, Box 951438, Los Angeles, CA 90095, USA
e-mail: lmartinez5@ucla.edu

and untapped paleoclimatic archive for California. Future work will focus on a latitudinal series of sag ponds to determine the spatiotemporal sequence and correlativity of SPEs in the sediment record.

Keywords Grain size · Sedimentology · Event deposition

Introduction and background

When you think of natural hazards and California, earthquakes dominate the narrative. But in terms of socioeconomic impact, floods are the single greatest natural hazard threat to California (Dettinger 2011; Porter et al. 2011; Corringham et al. 2022; Huang and Swain 2022). For example, in 1861–1862 AD, California experienced an historically unprecedented series of winter storms generating extreme precipitation and statewide flooding (Engstrom 1996). This 45-day period of record storms flooded nearly every major California metropolitan area at the time. Moreover, now dry lakes in the Mojave re-emerged, Tulare Lake expanded, and significant coastal erosion occurred along the California Coast (Porter et al. 2011; Reynolds et al. 2018). The USGS modeled this scenario (i.e., the ARkStorm, or ~1000-year event) as if it happened today and estimated the projected cost approximately 2×the estimated impact of the potential “big” San Andreas Fault earthquake (Porter et al. 2011). Future climate projections suggest that extreme precipitation accumulation amounts may increase by 10–40%, extreme precipitation variability will increase, and extreme events like that in 1861–1862 AD may increase in frequency by up to three-fold during the twenty-first century (Polade et al. 2017; Swain et al. 2018; Gershunov et al. 2019; Huang et al. 2020; Huang and Swain 2022).

At present, our knowledge of California’s flood history is derived from marine or coastal sediments (Fig. 1). Several important records illustrate flood events such as a 9000-year flood event history from Santa Barbara Basin (SBB; Schimmelmänn et al. 1998; Hendy et al. 2013, 2015; Du et al. 2018; Sarno et al. 2020), a 7000-year potentially flood-related turbidite sequence in the Santa Monica Basin (Romans et al. 2009), a mid-Holocene flood event layer in Lake Elsinore (Kirby et al. 2021), and evidence for the 1861–1862 AD over wash deposit from Carpinteria

Marsh (south of Santa Barbara, CA; Reynolds et al. 2018). Du et al. (2018) show that flood frequency and magnitude are in general positively correlated throughout the Holocene. Moreover, the frequency of floods tends to cluster and shows regional correlations to pluvials from terrestrial archives (Kirby et al. 2010, 2012, 2014, 2015; Hiner et al. 2016). More recently, Du et al. (2021) revealed that the SBB flood record shows a strong Holocene-scale connection to El Niño–Southern Oscillation (ENSO) variability and Pacific ocean–atmosphere dynamics. This relationship agrees with lower-resolution terrestrial records from California that show Holocene-scale couplings between ENSO and Pacific ocean–atmosphere dynamics for droughts and pluvials (Masters 2006; Covault et al. 2010; Miller et al. 2010; Kirby et al. 2014, 2015, 2023; Hiner et al. 2016; MacDonald et al. 2016).

Perhaps most revealing from the SBB flood record is the relatively subtle sediment signature associated with the 1861–1862 AD “ARkStorm-type” event. If event thickness is an approximate indicator of event magnitude (reasonable as a first approximation; Sabatier et al. 2022), the ARkStorm scenario is likely underestimating the scale of future SPEs and their associated flood risk in California. In fact, the SBB flood record is characterized by at least 30 flood-event layers that are thicker than the rather undersized 1861–1862 AD event (Du et al. 2018). This realization represents a potentially important mismatch between the geologically observed record and modeling output. Critical to predicting future flood scenarios is the ground-truthing of predictions and models in the geological record. We propose to address this very issue using sediments from a sag pond along the San Andreas Fault in the southern Carrizo Plain National Monument (Fig. 1). Moreover, despite a very well dated marine record offshore from Santa Barbara, the terrestrial spatiotemporal signature of SPE floods remains largely unconstrained.

Regional climatology

The climate of Southern California is Mediterranean—cool, wet winters and hot, dry summers (Bailey 1966). Year-to-year winter precipitation variability is related to tropical and north Pacific ocean–atmosphere dynamics and their modulation of

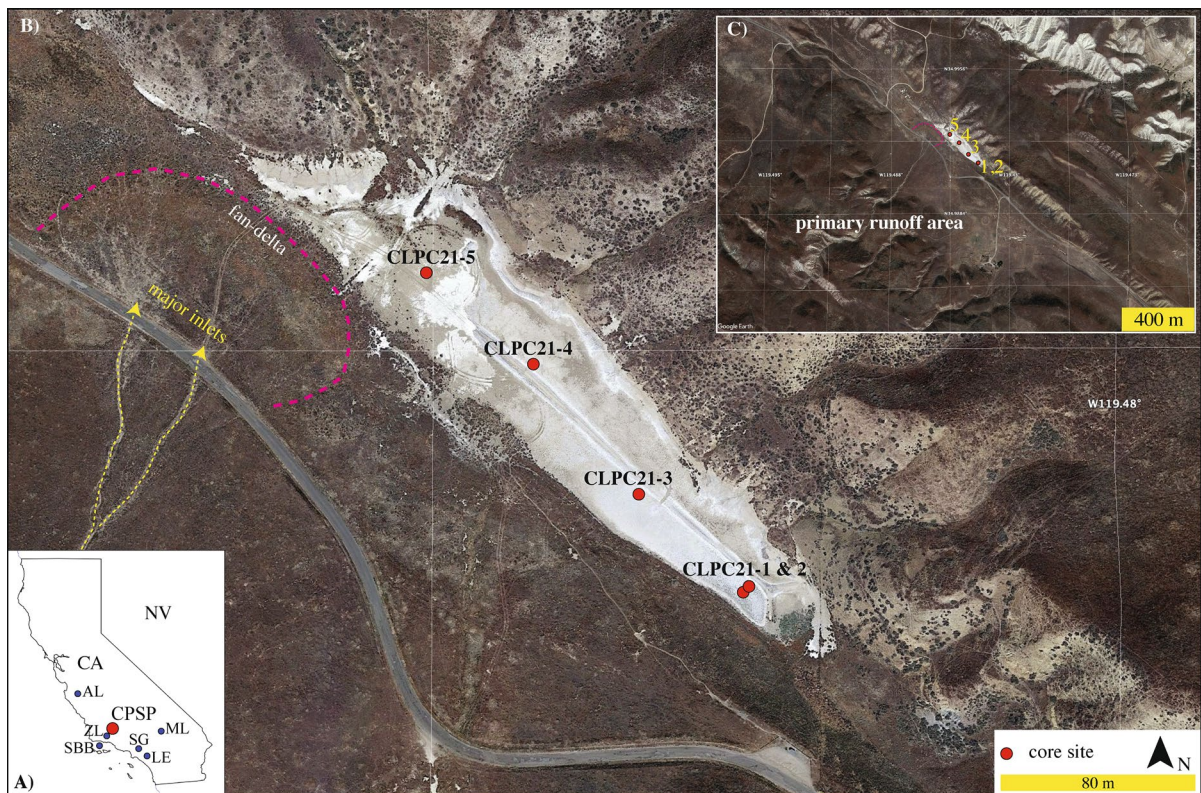


Fig. 1 **a** Regional and **b** local maps with core site locations (Google Earth Pro v.7.3.6.9345, 4/22/21 image date) and **c** major drainage area noted (see Supplementary material 1). **a** CPSP=Carrizo Plains Sag Pond, ZL=Zaca Lake (Kirby et al. 2014), AL=Abbott Lake (Hiner et al. 2016), SBB=Santa Bar-

bara Basin (Sarno et al. 2020), SG=San Gabriel regional tree rings (MacDonald et al. 2008; Meko et al. 2017), LE=Lake Elsinore (Kirby et al. 2010, 2018), ML=Mojave Lakes (Enzel et al. 1992; Miller et al. 2010; Honke et al. 2019)

the winter-storm track over the western US (Cayan and Peterson 1989; Castello and Shelton 2004; Hanson et al. 2006). For example, both ENSO and the Pacific Decadal Oscillation modulate the mean winter position of the eastern Pacific subtropical high and thus the average latitude of the Pacific winter storm track (Cayan and Peterson 1989; Castello and Shelton 2004; Hanson et al. 2006; Wise 2010, 2016). When conditions force the storm tracks further south, they produce higher-than-average precipitation and greater river discharge in Southern California, whereas a more northerly position results in lower-than-average precipitation and less river discharge (Cayan et al. 1998; Hanson et al. 2006; Gray et al. 2015).

In California, nearly all major floods in the twentieth century are attributed to winter season atmospheric river (AR) storms (Dettinger 2011; Dettinger et al. 2011; Ralph and Dettinger 2011; Konrad and

Dettinger 2017; Corringham et al. 2019). These narrow, moisture-rich plumes transport enormous quantities of water vapor from the tropics and subtropics into the mid-latitudes (Ralph and Dettinger 2011). ARs converge with coastal ranges, experience orographic lifting, and generate precipitation amounts several standard deviations above normal, often leading to landslides, debris flows, floods, and possibly incising new stream channels (Grant-Ludwig et al. 2010). Only land-falling hurricanes of the North Atlantic generate comparable precipitation amounts in North America (Dettinger et al. 2011). Although much less frequent than winter-season ARs, dissipating eastern tropical Pacific cyclones, such as Hurricane Kathleen in 1976, may impact the study area (Corbosiero et al. 2009). Currently, it is not possible to unequivocally differentiate the precipitation source of paleo-floods; however, statistically a winter-season

AR is more likely the cause of flooding at the study site than is a late-summer tropical cyclone.

Study site

The study site is a sag pond (hereafter Carrizo Plain sag pond; CPSP: N34°59'30.35"; W119°29'0.13") located along the San Andreas Fault (SAF) between the Temblor Range and the Caliente Range at 804 masl (Fig. 1). Sag ponds are topographic depressions formed along strike-slip faults; they are common along the SAF in California. Previous earthquake-interval research done on the SAF 36 km NW of our study site indicates that the recent average interval of rupture events is 88 ± 41 years with a slip rate of ~ 35 mm year⁻¹ (Akçiz et al. 2010; Grant-Ludwig et al. 2010). Rupture events can affect the sedimentology of sag pond sediments and will be considered when interpreting the site's sedimentology. Although the current lake surface area is small (~ 0.021 km²), the sag pond receives runoff from a large drainage basin (~ 9.2 km²; see Supplementary material 1). CPSP is also a terminal basin with no outlets. The drainage basin is highly asymmetric with most of the drainage originating from the south, west, and northwest sides of the lake (see Supplementary material 1). Deeply incised channels characterize the south, west, and northwest drainage basin. A fan delta-like feature is apparent along the lake's northwestern edge, connecting to a visually distinct channel despite construction of a road bisecting the channel (see Supplementary material 1). Although observational, the incised channels and fan delta-like feature suggest periods of active flow in recent times. The eastern side of the lake is steep and deeply incised, but it represents a much smaller drainage area. Google Earth historical imagery from 1985 to 2022 reveal instances of standing water in the southeastern sector (i.e., modern depocenter) of the lake as recently as February 2020. Notably, there are only two images from 1985 to 2002, so the breadth of the lake's modern hydrological fluctuations is poorly constrained. The local modern vegetation is predominantly a shrub and grassland community (Buck-Diaz and Evans 2011). Exotic grass species such as *Erodium* are common.

There are no climate data from the study site. As a result, we infer its climate from historical meteorological data from the Western Regional Climate

Center database using Taft, CA, as our comparison site (NWS Cooperative Network Number 048752, 1948–2008 AD, 17 km NNE of CPSP). Summer (JJA) temperatures average 26.7 °C; winter (DJF) temperatures average 10.4 °C. Average annual precipitation averages 137 mm with 105 mm (or 76.8%) of the total occurring between November and March.

Methods

Five sediment cores—CLPC21-1 to CLPC21-5—ranging from 125 to 156 cm in length were taken along the long axis of CPSP using a post-driver attached to a 4" diameter aluminum barrel (Fig. 1, Table 1). The cores were transported back to California State University, Fullerton where they were split lengthwise, visually described, and digitally photographed. Of the five sediment cores, we focused on CLPC21-04 (156 cm) for detailed analyses and age control, being the most complete core and with the thickest event units. In two of the five cores (CLPC21-01, -02), the core sediment separated during core extrusion (i.e., noted as core breaks in the photographs). Because the core is a single drive, we know that there is no missing sediment associated with the core break as the break occurs mid-core. Although the research focused on CLPC21-4, all five cores were examined using visual stratigraphy, magnetic susceptibility, and percent water content.

Age control for this study was determined on core CLPC21-4 using radiocarbon dating (accelerator mass spectrometry (AMS) ¹⁴C dating) on seventeen discrete microscopic and macroscopic (> 125 μm) organic materials (e.g., charcoal, seeds, insect parts). Samples were measured on the insoluble fraction for ¹⁴C at the University of California, Irvine Keck

Table 1 Study site core locations

Core ID	Latitude	Longitude
CLPC21-1	34 59'27.3"N	119 28'56.2W
CLPC21-2	34 59'27.4"N	119 28'56.1W
CLPC21-3	34 59'28.9"N	119 28'58.3W
CLPC21-4	34 59'31.0"N	119 29'00.4W
CLPC21-5	34 59'32.5"N	119 29'02.5W

Note: cores 1 and 2 were taken adjacent to one another within 2-m horizontal distance. Carrizo Lake Cores (804 m amsl)

Carbon Cycle AMS Facility (Table 2). All samples were treated with an acid–base–acid protocol (1N HCl and 1N NaOH, 75 °C) prior to combustion. Radiocarbon concentrations are given as fractions of the modern standard, $D^{14}C$, and conventional radiocarbon age, following the conventions of Stuiver and Polach (1977). Sample preparation backgrounds have been subtracted, based on measurements of ^{14}C -free wood. All results have been corrected for isotopic fractionation according to the conventions of Stuiver and Polach (1977), with $\delta^{13}C$ values measured on prepared graphite using the AMS spectrometer. Radiocarbon ages were converted to age in calendar years before present and age in Common Era (CE) using OxCal v.4.4.4 (Ramsey 2021) and the IntCal20 Northern Hemisphere radiocarbon age calibration curve from Reimer et al. (2020; Table 2). As our focus is on CE age, we also report the CE median, minimum, and maximum with the latter two ages reported at the 95.4% range (Table 2). We selected the range of CE years (min to max) for any given ^{14}C age using the highest percent value reported under the 95.4% probability distribution curve. ^{137}Cs was also measured in the upper 50 cm of core CLPC21-4 (Table 2). Finally, *Erodium* pollen were identified (presence vs absence) at various depth—based on initial ^{14}C dates to constrain their likely occurrence—at 10 depths from non-event (i.e., ambient) sediment units on core CLPC21-4 to determine the first appearance of the exotic grass for use as an independent age marker and to assess the ^{14}C ages (Table 2; Mensing and Byrne 1998; Kirby et al. 2014). All 1 cm³ pollen samples ($n=10$) underwent standard pollen-extraction procedures (Faegri et al. 1989; Bennett and Willis 2001). Tracer grains of *Lycopodium* were added during 10% HCl digestion (Batch #1031, Lund University). Pollen identifications were based on modern reference collections. *Erodium* grains were identified only to genus. Other pollen taxa present in the samples were noted, but not counted. Pollen preservation was poor in all samples, though only one sample was unusable.

Magnetic susceptibility (MS; $\times 10^{-7} \text{ m}^3 \text{ kg}^{-1}$) was measured at 1 cm contiguous intervals on sediment-filled individual 8 cm³ plastic cubes using a Bartington MS2 magnetic susceptibility meter on all five sediment cores. The same cubed samples were used to determine percent water content and percent dry bulk density. Using core CLPC21-4, 1-cm contiguous samples were combusted at 550 °C and 950 °C

for two hours to calculate the percent total organic matter (% TOM) and percent total carbonate (% TC), respectively (Dean 1974). Charcoal per 1-g dry sediment were counted on CLPC21-4 from 30 to 156 cm. The upper 30 cm were not counted for charcoal due to modern, near surface mud cracks that likely compromise the accuracy of the more-recent charcoal counts.

Grain size was measured at 1-cm contiguous intervals on CLPC21-4 following standard pretreatment protocols: 30–50 mL of 30% H_2O_2 , 10 mL of 1N HCl, and 10 mL of 1N NaOH (Leidemeijer et al. 2021). Grain size was determined using a Malvern Mastersizer 2000 grain size analyzer attached to a Hydro 2000G dispersion unit. A ten second sonication proceeded each analysis in the Hydro 2000G dispersion unit prior to analysis. A silica carbide polishing powder standard was run twice at the beginning of each day, once every ten samples, and once at the end of every day to evaluate the equipment's analytical stability and reproducibility over time ($n=4127$, average = 13.11 μm , standard deviation = 0.10 μm). All data are reported as volume percent and divided into 10 grain size intervals according to the Wentworth scale (Wentworth 1922) as well as d0.5 (0.5 = mean).

We utilized Principal Component Analysis (PCA) based on normalized data and Euclidean distance to explore the relationship between magnetic susceptibility, percent total organic matter, charcoal counts, and the ten grain size divisions ($n=124$ depths of shared data) on core CLPC21-4. To help confirm the statistical significance of the relationships between samples, we calculated a similarity profile (SIMPROF) permutation test. SIMPROF analysis enables us to test for structure in multivariate data and returns a p-value to determine whether the multivariate structure manifest in a group of samples are more or less similar to each other than would be expected if the data were random and lacked structure. A more detailed review of this technique can be found in Clarke et al. (2008) and Somerfield and Clarke (2013). All statistical analyses were conducted using PRIMER V7 (PRIMER-E, Plymouth, UK).

Results

Visually, all five cores are characterized by relatively massive, homogenous sediment (Fig. 2). Interrupting this homogeneity are several units that are visually

Table 2 All age control data from CLPC21-4 including ^{14}C , ^{137}Cs , and *Erodium*'s first appearance. Chronological data

UCIAMS #	Sample name	Depth (cm)	Fraction modern	\pm	D^{14}C (‰)	\pm	^{14}C age (BP)	\pm	Median (Cal Years Before Present)	Min	Max	Relative area under probability distribution	Median (CE)	Min (CE)	Max (CE)	OxCal v4.4.4, r:5 (95.4% probability) Percent under curve	Material dated	Ambient versus event
	Surface ^{137}Cs	0.5							-71				2021					Surface ^{137}Cs Event
		43.5							-13				1963					Event
266,117	CLPC21-4 59–60 cm seed 0.031 mg C	59.5	0.9704	0.0053	-29.6	5.3	240	45	278	256	333	0.374	1669	1615	1694	36.4	Single seed, charred	Event
273,601	CLPC21-4 80–82 cm-A	81.0	0.9819	0.0016	-18.1	1.6	145	15	135	60	117	0.284	1815	1832	1890	26.7	Charred seeds, all same type	Event
273,602	CLPC21-4 80–82 cm-B 0.14 mg C	81.0	0.9825	0.0017	-17.5	1.7	140	15	109	58	118	0.363	1842	1831	1893	34.7	Charred seeds, all same type	Event
273,603	CLPC21-4 86–87 cm	86.5	0.9724	0.0016	-27.6	1.6	225	15	181	279	305	0.491	1676	1645	1673	49.6	Charred seeds, all same type	Ambient
266,118	CLPC21-4 87–88 cm seeds 0.05 mg C	87.5	0.9701	0.0035	-29.9	3.5	245	30	292	268	320	0.546	1659	1630	1682	53.5	3 Nice seeds, charred	Ambient
273,604	CLPC21-4 89–90 cm-A 0.11 mg C	89.5	0.9847	0.0025	-15.3	2.5	125	25	110	10	150	0.712	1841	1800	1940	67.8	Insect parts?	Ambient
273,605	CLPC21-4 89–90 cm-B 0.046 mg C	89.5	0.9769	0.0074	-23.1	7.4	190	70	179	0	318	0.965	1770	1630	mod-ern	91.7	Insect parts?	Ambient
273,606	CLPC21-4 89–90 cm-C 0.23 mg C	89.5	0.9734	0.0016	-26.6	1.6	215	15	170	151	174	0.449	1774	1762	1800	52.7	Single Charred seed	Ambient

Table 2 (continued)

UCIAMS #	Sample name	Depth (cm)	Fraction modern	±	D ¹⁴ C (‰)	±	¹⁴ C age (BP)	±	Median (Cal Years Before Present) Calib v 8.2	Min	Max	Relative area under probability distribution	Median (CE)	Min (CE)	Max (CE)	OxCal v4.4.4, r:5 (95.4% probability) Percent under curve	Material dated	Ambient versus event
266,119	CLPC21-4 93–94 cm seeds 0.19 mg c	93.5	0.9729	0.0018	–27.1	1.8	220	20	181	151	187	0.454	1761	1762	1800	46.2	2 Charred nice seeds	Ambient
UCLA	CLPC21-4 107–108 cm Exotic pollen	107.5											1755	1750	1765		First appearance of Erodium	Ambient
266,120	CLPC21-4 115–116 cm seed 0.11 mg C	115.5	0.9541	0.0020	–45.9	2.0	375	20	452	428	496	0.658	1499	1452	1522	62.8	Single charred seed	Event
266,121	CLPC21-4 127–129 cm char 0.058 mg C	128.0	0.9805	0.0034	–19.5	3.4	160	30	164	165	231	0.33	1784	1719	1786	31.5	Random charred woody pieces	EU 2
266,122	CLPC21-4 129–130 cm char 0.12 mg c	129.5	0.9763	0.0018	–23.7	1.8	195	15	181	148	190	0.424	1767	1735	1804	61.1	Nice char-coal	EU 2
266,123	CLPC21-4 130–131 cm char .18mgC	130.5	0.9511	0.0018	–48.9	1.8	405	20	484	448	508	0.927	1467	1442	1500	88.9	Nice char-coal	EU 2
266,124	CLPC21-4 131–132 cm char .18mgC	131.5	0.9709	0.0017	–29.1	1.7	235	15	289	282	307	0.626	1661	1644	1668	61.7	Nice char-coal	EU 2
266,125	CLPC21-4 132–133 cm char 0.13 mg C	132.5	0.9633	0.0019	–36.7	1.9	300	20	395	358	440	0.749	1556	1510	1594	71.3	Nice char-coal	EU 2

Table 2 (continued)

UCIAMS #	Sample name	Depth (cm)	Fraction modern	\pm	D ¹⁴ C (‰)	\pm	¹⁴ C age (BP)	\pm	Median (Cal Years Before Present)	Min	Max	Relative area under probability distribution	Median (CE)	Min (CE)	Max (CE)	OxCal v4.4.4, r:5 (95.4% probability) Percent under curve	Material dated	Ambient versus event
266,126	CLPC21-4 153–154 cm char 0.054 mg C	153.5	0.9582	0.0033	-41.8	3.3	345	30	391	313	415	0.625	1560	1470	1637	95.4	Single charcoal wood	Ambient
273,607	CLPC21-4 153–155 cm 0.30 mg C	154.0	0.9621	0.0016	-37.9	1.6	310	15	395	359	439	0.796	1556	1514	1591	76	Mixed charcoal	Ambient

(e.g., darker), sedimentologically (e.g., coarser), and structurally (e.g., thicker and with sharp lower boundaries) distinct. Most notable are two units near the bottom of each core—hereafter, Event Unit 1 (EU 1: 151–141.5 cm) and Event Unit 2 (EU 2: 139–128 cm; Fig. 2). From north to south in the basin, EU 1 and EU 2 thin and become less coarse. There are other visually distinct units nearer the mid-to-top of each core, although much thinner than EU 1 and EU 2 and not as easy to correlate across cores. Finally, each core shows a darker, massive unit of varying thickness above EU 2 (Fig. 2). To avoid subjective interpretation of the PCA data, we focus on the two bottom units only (i.e., the most extreme negative PC1 values (EU 1 and EU 2)), which are visually correlated across the core sites. Moreover, we limit our detailed sedimentological and chronological efforts on the longest core (CLPC21-4), which is the only core to capture EU 1 and EU 2 in their entirety and with thick enough bedding to extract meaningful sedimentological information (i.e., >1 cm or >one point of data; Fig. 3). Cores CLPC21-1, -2 also capture both EU 1 and EU 2 in their entirety; however, they are much thinner and cannot provide multi-depth sedimentological analyses.

Figure 3 shows all the sediment data including the pertinent age control data for core CLPC21-4. To evaluate these data objectively and statistically in terms of sedimentological characteristics, we utilized Principal Component Analysis (PCA) based on normalized data and Euclidean distance to explore the relationships between magnetic susceptibility, percent total organic matter, charcoal counts, and the 10-grain size divisions ($n=124$ depths of shared data; see Supplementary material 2). The top 30 cm of data was not included in the PCA as it did not include charcoal data. PC1 axis accounts for 52.7% of the variation within the samples. The PCA plot shows that the positive PC1 axis is associated with MS ($\mu=1.8$, $\sigma=0.3$), % TOM ($\mu=8.80$, $\sigma=1.49$), % clay ($\mu=17.13$, $\sigma=3.26$), % very fine silt ($\mu=24.03$, $\sigma=3.15$), % fine silt ($\mu=24.90$, $\sigma=3.54$), and % medium silt ($\mu=19.79$, $\sigma=3.52$); whereas, the negative PC1 axis is associated with charcoal ($\mu=23.79$, $\sigma=43.56$), % coarse silt ($\mu=18.91$, $\sigma=6.72\%$), % very fine sand ($\mu=19.78$, $\sigma=10.59$), % fine sand ($\mu=10.12$, $\sigma=8.44$), % medium sand ($\mu=4.80$, $\sigma=9.46$), % coarse sand ($\mu=2.71$, $\sigma=7.07$), and % very coarse sand ($\mu=0.44$, $\sigma=1.98$). PC2 is not

addressed as it accounts for only 19.4% of the variance, and it did not add significant (or meaningful) information to our interpretation.

Plotting PC1 shows seven units where the PC values are less than zero being characterized by coarser sediment particularly coarse silt, very fine, and fine sand. As the PC1 values become more negative, the content of coarse and very coarse sand and the occurrence of charcoal both increase; although, charcoal is generally found only at the top of the most PC1-negative units. As an additional analysis of the differences between the positive and negative PC1 data, we plotted percent clay versus the five sand classifications as well as percent total sand (Fig. 4). For each comparison, there is a notable difference between clay content and sand sizes for the PC1 negative versus PC1 positive value sediments. PC1 negative values are consistently coarser in all sand-size fractions than are PC1 positive value sediments. Although four negative PC1 units are especially prominent in core CLPC21-4 (i.e., 151–141.5 cm, 139–128 cm, 75–68 cm, and 48–42 cm), we focus on the two lower units (EU 1 and EU 2) because they are characterized by the most negative PC1 values, they are sedimentologically and visually distinct, they are visually correlated across all five core site locations, and they are thick enough to extract meaningful sedimentological information (i.e., >1 cm or >one point of data per event unit). This conservative approach to interpreting the PCA results reduces interpretative subjectivity and over-interpretation of the less prominent PC1-negative units.

Both EU 1 and EU 2 are characterized by decreases in magnetic susceptibility, total organic matter, and percent clay, and increases in percent very fine and fine sand (Fig. 5). However, EU 1 also shows an increase in percent medium, coarse, and very coarse sand; whereas, EU 2 shows only a small increase in percent medium sand and an absence of coarse and very coarse sand. Overall, EU 1 is considerably coarser than EU 2; however, EU 1 also contains a spike in percent clay and magnetic susceptibility mid-event at 146–145 cm, apparent as a visually lighter colored layer in the digital photograph (Fig. 5). Structurally, both EU 1 and EU 2 show sharp lower boundaries with normal grading to finer sediment up-core to the event unit's upper boundary. EU 2 also contains well-defined-to-faint laminae between 136 and 130 cm; similar laminae are not observed

in EU 1 except for the thin clay layer noted above. Finally, charcoal content increases slightly at the top of EU 1, while it rises sharply to the highest values in the core in the upper section of EU 2.

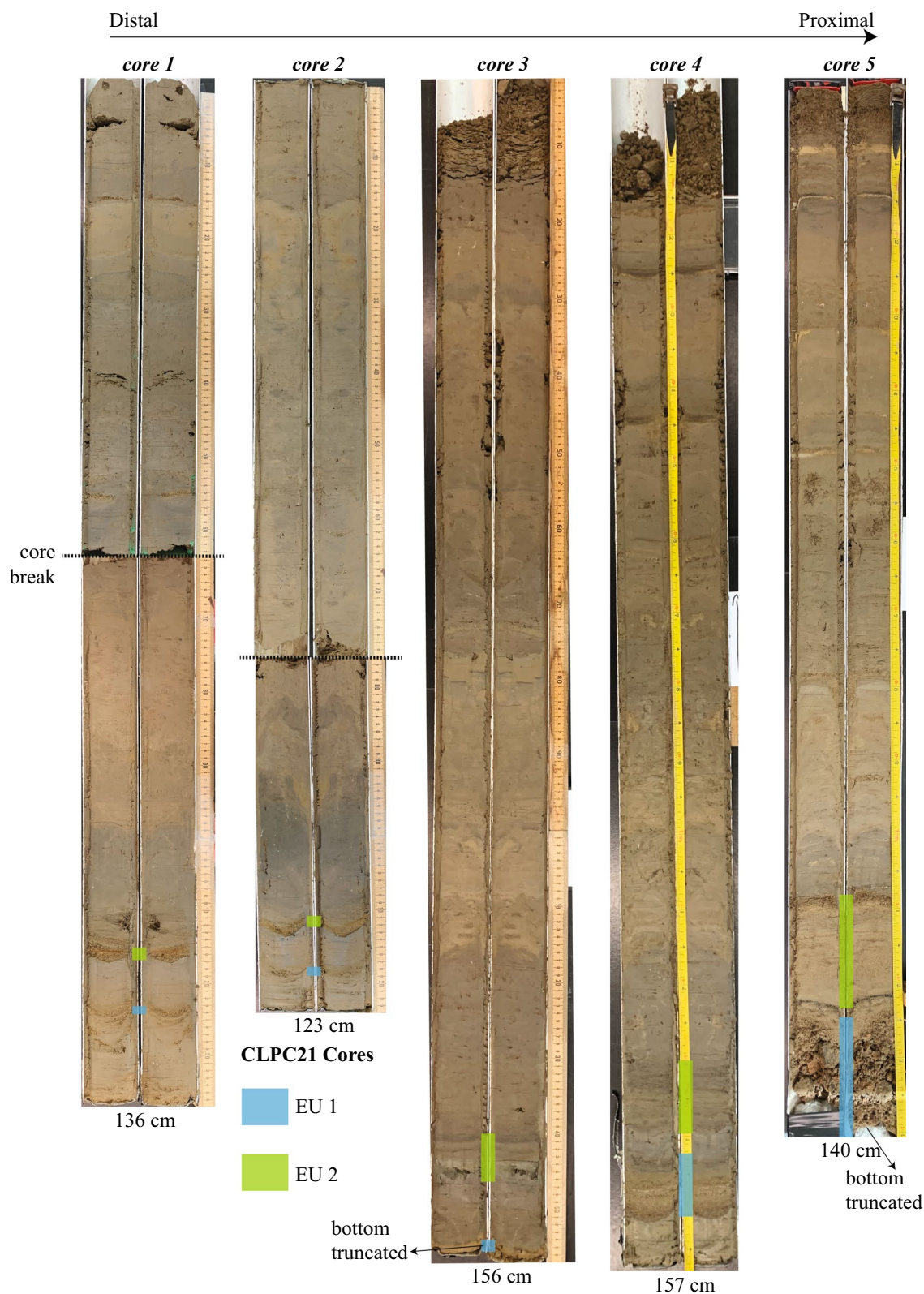
All age control data are shown on Fig. 6 and Table 2 and Supplementary material 3. The surface age was assigned modern or 2021 CE. The peak in ^{137}Cs occurred at 44–43 cm, which was assigned an age of 1963 CE. We used the radiocarbon results to identify the zone in which *Erodium* should first appear (see Supplementary material 3). *Erodium*'s first appearance is at 108–107 cm and was assigned an age of 1755 CE (range: 1750–1765 CE) based on Mensing and Byrne (1998) for the Santa Barbara region. Finally, an age model was not constructed for core CLPC21-4 because our focus is on the timing of EU 1 and EU 2 and not the core's complete depositional history.

Discussion

Statistics and depositional interpretations for EU 1 and EU 2

We focus on the grain size, specifically, to interpret these depositional environments as changes in grain size in lacustrine environments reflect well-established water energy-grain size dynamics such as changes in water depth, distance from the shore zone, and grain size-energy dynamics associated with runoff from the drainage basin (Anderson 1977; Davis and Ford 1982; Håkanson and Jansson 1983; Hilton 1985; Dearing 1991, 1997; Blais and Kalff 1995; Kirby et al. 2010, 2015, 2018; Bird et al. 2017; Pribyl and Shuman 2017; Shuman and Serravezza 2017). In general, finer grain sizes are deposited in lower energy environments, such as a lake's depocenter or its most distal point from the shoreline or sediment source; whereas, coarser sediments are generally associated with higher energy shoreline environments or event deposition caused by high energy processes such as precipitation-related runoff events (Anderson 1977; Dearing 1997; Brown et al. 2002; Kirby et al. 2010, 2014, 2015, 2021, 2023; Pribyl and Shuman 2017; Sabatier et al. 2022).

As previously noted, PC1 axis accounts for 52.7% of the variation within the samples with the positive PC1 axis associated with above average MS, % TOM,



◀**Fig. 2** All five core photographs with Event Units 1 and 2 highlighted (i.e., thickness of highlight=thickness of event unit). Core depth is shown at the bottom of each core photograph. Cores are arranged from proximal to the current source (core 5) to distal (cores 1 and 2; Fig. 1 and Supplementary material 1). Event Unit 1 is truncated in cores 3 and 5 based on depth of core penetration, and there true thickness is unknown

% clay, % very fine silt, % fine silt, and % medium silt and the negative PC1 axis associated with above average charcoal, % coarse silt, % very fine sand, % medium sand, % coarse sand, and % very coarse sand. This dichotomy in sediment type suggests that two depositional environments dominate the sag pond record. The dominance of finer grain sizes associated with positive PC1 values suggests a low energy environment wherein sediment is deposited, accumulated, and preserved, likely in standing water or intermittent lake conditions. As a result, we interpret positive PC1 values as representative of *ambient* sedimentation associated with non-event processes such as playa or lacustrine deposition. For this paper, we are not concerned with the ambient sediments except for their value in focusing our selection of depths for the presence vs. absence of *Erodium*. Punctuating these periods of ambient sedimentation are several coarse-grained sediment units (negative PC1 values)—the focus of this paper.

Coarser sediments dominate the negative PC1 values suggesting a higher energy depositional environment such as shoreline migration via changes in water depth, precipitation-related runoff (i.e., event sedimentation), concentration of coarse sediment via deflation, or earthquake disturbances. Although the PCA identifies 7 units where the PC values are less than zero (Fig. 3), two of the negative PC1 units are markedly different—EU 1 and EU 2 (Figs. 3 and 5). EU 1 and EU 2 are noteworthy for several reasons: (1) they are the most negative PC1 intervals, (2) they are thick enough to extract meaningful sedimentological information (i.e., > 1 cm or > one point of data per event unit), (3) they have erosional lower boundaries, (4) they contain the coarsest sediment, (5) they are normally graded, (6) they contain low % TOM and lower MS values, (7) they reveal an increase in charcoal near their upper boundary, and (8) they are visually correlated across all five cores at the study site. This combination of criteria suggests high energy deposition across the basin with diminishing energy from source (core 5) to sink (cores 1 and

2; Fig. 1; Sabatier et al. 2022). We contend that the most likely explanation for EU 1 and EU 2 are precipitation-related runoff events generated by SPEs. High intensity flow into the sag pond explains the erosional bases that characterize EU 1 and 2, as described for a mid-Holocene flood event in Lake Elsinore (Kirby et al. 2021). The thinning of the events from source (core 5) to sink (cores 1 and 2) indicates a progressive loss of energy as the runoff event flows down the long axis of the sag pond—a key criterium for discerning event origin (Sabatier et al. 2022). Normal grading is often associated with rapid deposition of sediment in aqueous environments wherein water–sediment energy dynamics generate grain-size separation (Wilhelm et al. 2012; Smith et al. 2019; Sabatier et al. 2022). Evidence for laminae, especially in EU 2, suggest progressive energy loss and grain-size separation during sediment deposition (Sabatier et al. 2022). The presence of a thin clay layer in EU 1 suggests pulsed sedimentation, perhaps concurrent events, and favor subaqueous deposition allowing the finest sediment (i.e., clay) to settle and accumulate. The charcoal peaks near the top of EU 1 and 2 also suggest that the least dense materials (i.e., organic debris) were deposited as the flow ceased and the slow settling of low-density detritus commenced. The latter also favors deposition in a subaqueous environment. The large age range of charcoal dated in EU 2 suggests significant erosion of the drainage basin, tapping into older stratum containing older charcoal and/or erosion of old charcoal sitting on the landscape. Low organic contributions suggest dilution of organics via higher clastic sediment contributions during event deposition and/or post-depositional oxidation of the organics. Low MS values within the event units suggest a change in the mineralogy of event vs. ambient sedimentation and/or post-depositional alteration of magnetic minerals. Based on the above evidence, EU 1 and EU 2 are interpreted as water-rich, sediment laden flows that likely generated turbidite-like units upon deposition, generated by precipitation-related runoff events, most likely into standing water (Fig. 5). However, we cannot unequivocally rule out that these event units were deposited on a playa surface as a surface flow event without the presence of significant standing water. In either scenario, the genesis remains linked to precipitation-related runoff in response to a SPE.

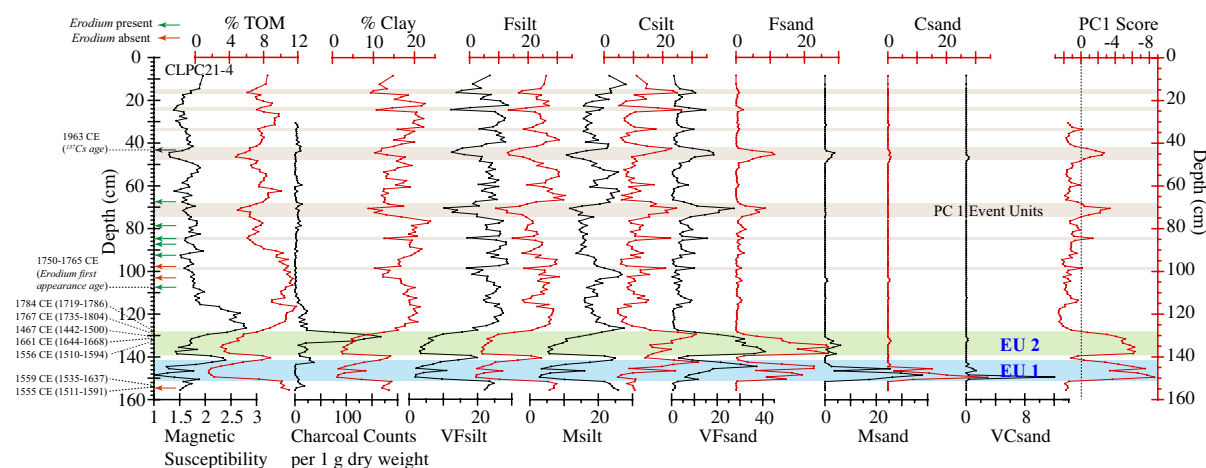


Fig. 3 Core CLPC21-4 with analyses versus depth. Key ages relevant to our discussion are shown to the far left in calibrated years CE with the 95.4% confidence range. Presence or absence of *Erodium* is shown by green arrows (present) and red arrows (absent). ^{137}Cs age is noted by black arrow; however, the Cs age is within an event unit is considered unreliable. All event units as identified by negative PC1 values are highlighted in beige except for EU 1 (blue) and EU 2 (green)=Event Unit 1 and Event Unit 2. From left to right:

magnetic susceptibility ($\times 10^{-7} \text{ m}^3 \text{ kg}^{-1}$), percent total organic matter, charcoal counts per 1 g dry weight, percent clay, percent very fine (VF silt) silt, percent fine (Fsilt) silt, percent medium (Msilt) silt, percent coarse (Csilt) silt, percent very fine (VF sand) sand, percent fine (Fsand) sand, percent medium (Msand) sand, percent coarse (Csand) sand, percent very coarse (VC sand) sand, and PC1 values. Grain size intervals according to the Wentworth scale (Wentworth 1922)

We also present, and refute, the three most reasonable alternative explanations for EU 1 and 2. The first alternative explanation for our two EUs is that they reflect a sedimentological response to sustained drought and the subsequent progradation of the shore zone across the core site (i.e., lake-depth shallowing; Kirby et al. 2018, 2023). If true, we expect to see a gradual change from fine grained clays and silts associated with a deeper water, low energy environment to coarser sandy silt and/or sand associated with a shallower water, high energy environment. As noted, the basal contacts for EU 1 and 2 are abrupt and erosive, and the units are normally graded (both units) with evidence for well-defined-to-faint laminae (only EU 2). We contend that this abrupt and erosive transition to coarse sediment is not consistent with a sustained progradation of the shore zone basinward in response to a slow lake-level regression. As a small sag pond, changes in lake level are likely rapid—based on modern observations—and this rate of change will exceed the response/equilibrium time for establishing a wholly new grain size-energy depositional environment. Moreover, the sag pond is extremely narrow across its long axis (<70 m) and likely would not record rapid and subtle changes in the position of

the littoral zone, as the distance between the lake's depocenter and shore is horizontally insignificant. On-site surface analysis as well as lidar imagery from the study site by Bevis and Hudnut (2005) reveal no observable beaches or stranded beaches to indicate prior, sustained highstands. Consequently, we do not think that EU 1 and 2 are shore-zone deposits associated with a prolonged drought or lake-level lowstand. As a result of these observations and reasonings, we rule out shore-zone progradation as an explanation for the EU 1 and 2.

Our second alternative explanation is that the event layers represent an encroachment of the fan-delta observed at the northwest side of the sag pond. Fan-deltas represent the distal portion of an alluvial fan where the fan meets and interacts with a standing body of water. They generally contain poorly sorted, coarse sediment, lack grading, and show both lateral and vertical heterogeneity (McPherson et al. 1987). We do not favor this origin for three reasons. First, EU 1 and EU 2 are well-sorted with normal grading, and they express lateral and vertical coherence across the basin. Second, fan-delta migration likely requires a significant period—decades to centuries—to form as well as a period of relatively persistent runoff to

move, establish, and deposit the fan-delta. Third, fan-deltas, by definition, require a body of standing water. During a period of sustained wetness (i.e., pluvial), as lake level rises, the fan-delta system will not prograde but retreat upland in response to the change in base-level (i.e., the lake-level transgression). For these reasons, we do not favor the interpretation that our event units (EU 1 and EU 2) represent fan-delta migration.

Our third alternative explanation for EU 1 and 2 is a seismogenic origin, such as a sand blow (i.e., vertical sand migration via seismogenic liquefaction) or seismite (i.e., soft sediment-deformation features associated with seismogenic, subaqueous shaking; Sabatier et al. 2022). We contend that a seismic origin is unlikely for several reasons. First, both EU 1 and 2 lack typical soft sediment-deformation features traditionally associated with lacustrine seismites (Bowman et al. 2004; Montenat et al. 2007; Sabatier et al. 2022). On the contrary, they are both normally graded and retain evidence, such as laminae in EU 2, for grain-size separation associated with water-energy dynamics during the flow of a water-rich, sediment-laden medium. Second, both units thin from source to sink suggesting a progressive loss of energy that is not readily explained by seismogenic processes such as a seismite (Migowski et al. 2004; Sabatier et al. 2022). Third, a seismite caused by shaking of the basin will not necessarily introduce coarse grains as it will only rework that sediment already in the basin. Not only are EU 1 and 2 coarser grained than the ambient sediment, but each unit becomes progressively finer and thinner from source (core 5) to sink (core 1). Fourth, EU 1 and 2 are characterized by abrupt, erosive lower boundaries, which cannot be easily explained via seismogenic processes, such as a sand blow. Therefore, we suggest that a seismic origin is very unlikely for EU 1 and EU 2.

EU 1 and EU 2 timing and the Little Ice Age

Initial depth selection for ^{14}C age control preceded completion of the sediment analyses and was based on visual inspection of the core and initial charcoal counts. As a result, six of the seventeen radiocarbon ages were extracted from ambient sediment units as defined by positive PC1 values (Table 2). To determine the age of EU 1, we focus on the ages collected from ambient sediment below the EU 1's erosional base (Figs. 5 and 6). Charcoal from 154

to 153 cm and combined 155 to 153 cm provide a range from 1470 to 1640 CE and 1510 to 1590 CE, respectively, at the 95.4% probability distribution under the calibration curve (Table 2). If the event's erosional base reflects the removal of sediment during sediment emplacement, we consider these ages to reflect the event's maximum age and likely younger when sediment erosion is considered. As a result, we assign a maximum age for EU 1 at 1470 CE and a minimum age at 1640 CE. Based on this range, it is possible that EU 1 represents the terrestrial equivalent to the 1525 CE SBB flood event.

Eleven of the seventeen ^{14}C ages were subsequently identified as occurring in event sediment units as defined by negative PC1 values (Table 2 and Fig. 6). The ages within event sediments are likely reworked and represent a variety of materials and their respective ages on the landscape at the time of erosion. Despite this reworking, we can infer important information about the event's age by examining the distribution of ages in the event unit. The youngest material dated within an event provides a maximum age for the event unit, assuming that it is more difficult to rework younger material into older sediments. Using this rationale, the youngest age in an event unit necessarily requires that the surface age of the landscape undergoing erosion was at least as old as the youngest date. For example, EU 2 contains five ^{14}C ages from detrital charcoal or charred wood (Table 2 and Fig. 6). These ages ($n=5$) range from 1440 to 1800 CE (Table 2). As a result, we infer a maximum limiting age for EU 2 using the distribution of ages from the youngest sample. The youngest sample occurs at 129–127 cm with a minimum to maximum age range of 1740–1800 CE at the 95.4% probability distribution under the calibration curve. Consequently, we suggest that EU 2 is likely no older than 1740 CE and no younger than 1800 CE (Figs. 5 and 6). Moreover, our suggested age for EU 2 is independently supported by the first occurrence of *Erodium* at 108–107 cm ranging from 1750 to 1765 CE (Mensing and Byrne 1998). Assuming the *Erodium* age—as determined from SBB marine sediments—is reasonably applicable to the Carrizo Plains (100 km NNE of SBB), we can additionally constrain the age of EU 2 to 1740 to 1765 CE. Whether the former (1740–1800 CE) or latter (1740–1765 CE), the inferred age of EU 2

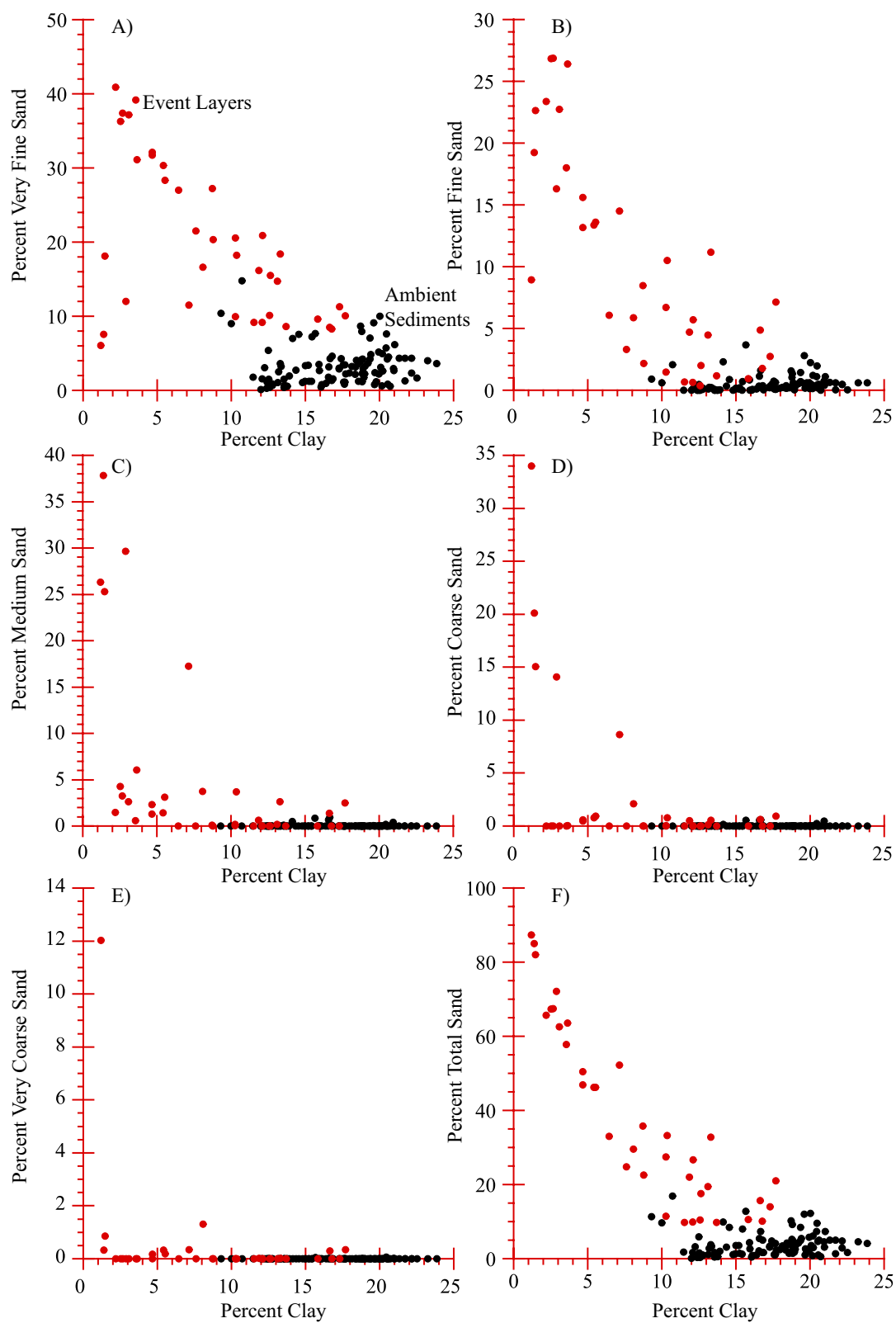


Fig. 4 Scatter plots comparing various sand sizes (including percent total sand) versus percent clay based on PC1 values. Negative PC1 values = event sedimentation (red circles); positive PC1 values = ambient sedimentation (black circles). **a** percent clay versus percent very fine sand, **b** percent clay versus percent fine sand, **c** percent clay versus percent medium sand, **d** percent clay versus percent coarse sand, **e** percent clay versus percent very coarse sand, and **f** percent clay versus percent total sand

is remarkably similar in age to the 1760 CE flood layer identified in the SBB (Sarno et al. 2020).

Notably, EU 1 and EU 2 are separated by only 2 cm of ambient sediment in core 4. Because EU 2 is characterized by a sharp, erosional base, it can be inferred that some amount of sediment (i.e., time) was removed during event deposition and the 2 cm of remnant ambient sediment was originally thicker (i.e., more time between EU 1 and 2). Without knowing the sedimentation rate and acknowledging the fact that our study cores are punctuated by event sedimentation, it is difficult to estimate the amount of time separating EU 1 and EU 2 and the amount of sediment removed via erosion during EU 2. However, the thickness of the ambient sediment unit between EU 1 and 2 increases as the core distance from the source lengthens, suggesting a reduction in erosive power from source to sink (core 5 = proximal, core 1 and 2 = distal; Fig. 2). This observation provides additional and independent support that EU 1 and EU 2 are separated by a measurable period of time, and they are not genetically linked by a temporally correlative series of events. As a result, our best estimate for EU 1 is between 1470–1640 CE and EU 2 between 1740 to 1765 CE.

The Little Ice Age (LIA) was a period of climate change during the late Holocene between 1450–1850 CE (IPCC age range, Masson-Delmotte et al. 2013), characterized by changes in temperatures, hydroclimates, and atmospheric/oceanic circulation (Haug et al. 2001; Chiang and Friedman 2012; Koutavas and Joanides 2012; Rustic et al. 2015; Cvijanovic et al. 2017; Loisel et al. 2017; Slawinska and Robock 2018; Lapointe and Bradley 2021). In Southern California, several paleoclimatic archives characterize the LIA as reflecting cooler and/or wetter hydroclimates. For example, lake sediments from Abbott Lake (1450–1570 CE, 1710–1775 CE; Hiner et al. 2016), Zaca Lake (1450–1500 CE, 1580–1710 CE; Kirby et al. 2014), and Lake Elsinore (1450–1530

CE, 1580–1610 CE, 1670–1700 CE, 1750–1780 CE; Kirby et al. 2010, 2018) suggest enhanced precipitation-related runoff during the LIA. At the same time, ephemeral lakes in the Mojave Desert re-emerged (e.g., Silver Lake and Cronese Lakes) and wetlands expanded (i.e., Soda Lake; ~1650 CE; Enzel et al. 1992; Miller et al. 2010; Honke et al. 2019). East of the Mojave in Arizona, Ely (1997) observed a sharp increase in flood frequency after 1450 CE. Tree ring reconstructed water year precipitation for the San Gabriel drainage basin shows more frequent, above-average precipitation during the LIA (Meko et al. 2017). Similarly, tree ring Palmer Drought Severity Index (PDSI) reconstructions suggest sustained periods of less drought and a generally above-average PDSI for Southern California, except between 1580–1720 CE (MacDonald et al. 2008). In the SBB, Sarno et al. (2020) identified only two floods within the LIA (1450–1850 CE *sensu stricto*) at 1525 and 1760 CE. The 1525 CE SBB flood-event layer is the second thickest event layer (out of 12) in the past 2000 years (Sarno et al. 2020).

Our research from the Carrizo Plains reveals two event units likely related to SPEs that are contemporaneous with the LIA chronozone (i.e., IPCC age range, Masson-Delmotte et al. 2013). Without older sediment studies at our site, we cannot say with certainty that the Carrizo Plains were wetter-than-average during the LIA. However, based on the spatiotemporal signature of a wetter-than-average LIA across Southern California, it is not unreasonable to assume that the Carrizo Plains were also wetter-than-average during the LIA. Future work on longer Carrizo Plains sediment cores is required to test the latter statement. As we note above, our data suggest another five PC1 negative event units in the Carrizo Plains study site. Without additional age control per core and additional in-depth analyses per core, we cannot—at this time—assign a definitive origin to these additional, younger five PC1 negative units.

Broader implications

The results of this study demonstrate the utility of sag ponds as possible paleoclimatic archives. These ponds may prove particularly useful for documenting SPEs in the geologic record due to their focused drainage basins and their occurrences in regions devoid of more traditional lake environments.

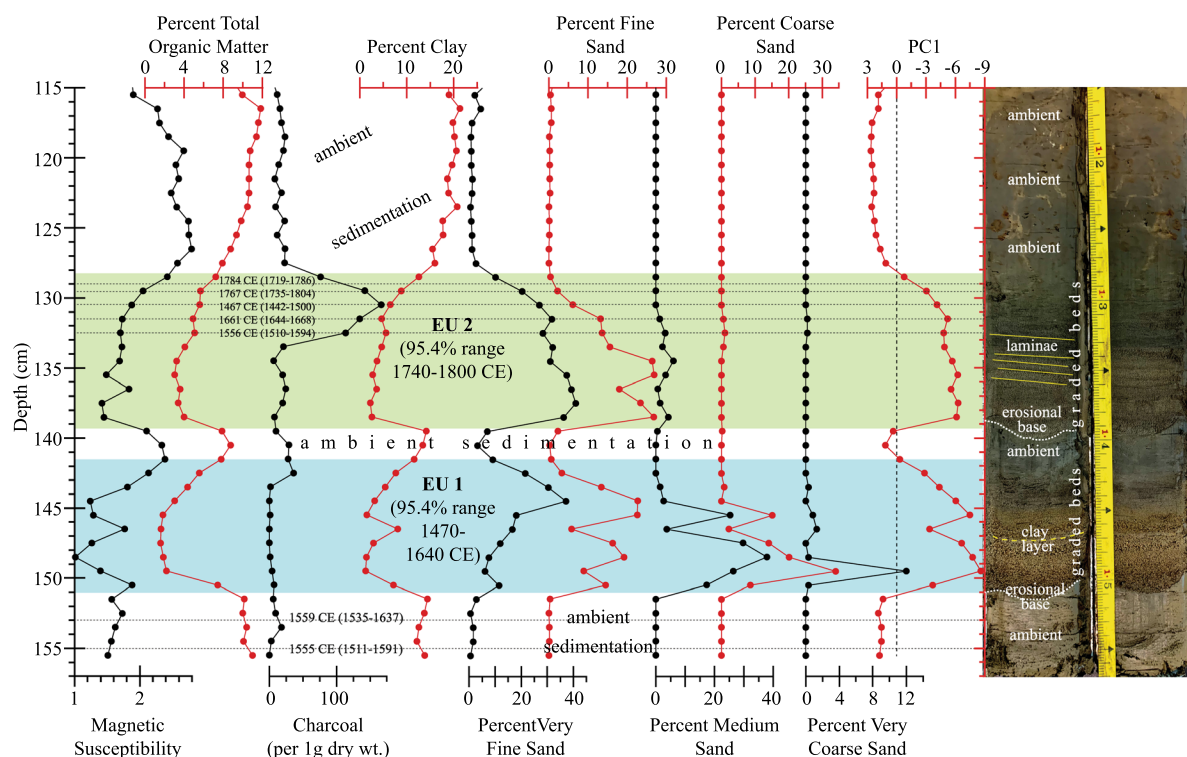


Fig. 5 A close-up view of EU 1 and EU 2 in core CLPC21-4 (split halves of the same core) with analyses versus depth and digital photograph (colors enhanced to highlight EU 1 and 2). Key ages relevant to our discussion are shown in calibrated years CE with the 95.4% confidence range. The best-estimate age range is shown for both EU 1 and 2 in the colored boxes.

Coastal and marine archives, such as SBB, more likely integrate regional runoff events related to SPEs from throughout the Southern California region and its more extensive drainage basin. However, given the narrow width of SPEs (specifically ARs), the SBB flood events do not necessarily represent the whole region and highlight the necessity to locate and study the spatiotemporal signature of SPE floods recorded in terrestrial archives. Sag ponds have the potential to improve our understanding of past SPE storm tracks in addition to SPE storm frequency. Adding records from other sag ponds in this region will allow us to disentangle the spatial signature of SPEs across coastal California. Sag ponds may prove a valuable and generally untapped paleo archive that can improve our ability to distinguish the spatiotemporal signatures of SPEs in the geologic past.

From left to right: magnetic susceptibility ($\times 10^{-7} \text{ m}^3 \text{ kg}^{-1}$), percent total organic matter, charcoal counts per 1 g dry weight, percent clay, percent very fine sand, percent fine sand, percent medium sand, percent coarse sand, percent very coarse sand, and PC1 values. Grain size intervals according to the Wentworth scale (Wentworth 1922)

Conclusions

Our study using sediments from a small sag pond along the SAF provides evidence for at least two SPE flood units over the past 500 years, within the chronozone of the Little Ice Age. Alternative explanations such as shore-zone progradation in response to sustained drought, fan-delta migration, or seismogenic origins are not supported by the visual and sedimentological data. Age control as determined from both event sediments and ambient sediments was used to constrain the events' timing. Based on ambient sediments below the erosive base of EU 1, we assign a temporal range between 1470 and 1640 CE, possibly correlative to the 1525 CE SBB flood unit. Using the distribution of ^{14}C ages from within EU 2 and the first occurrence of *Erodium*, we assign a range between 1740 and 1765 CE, possibly correlative to

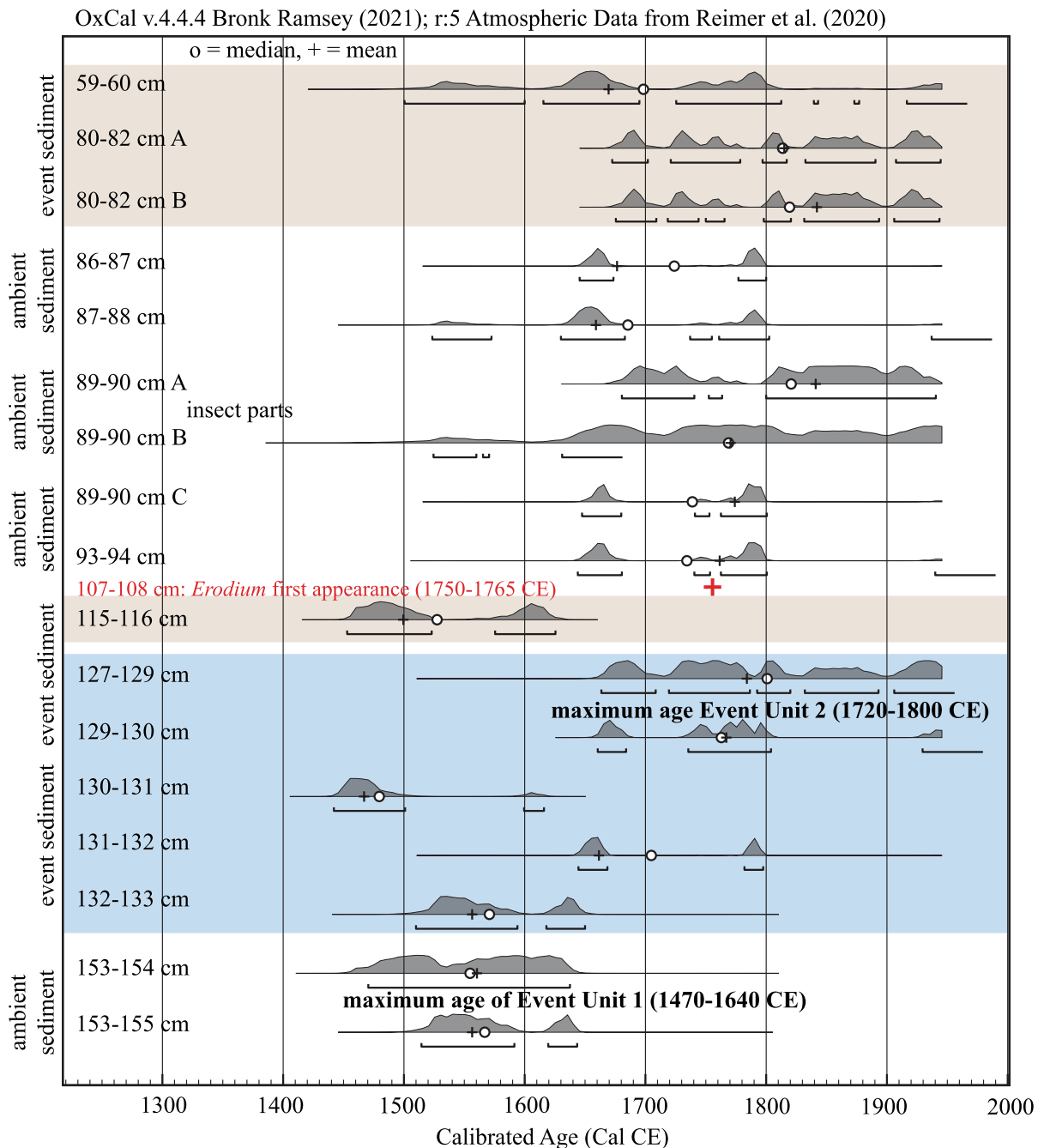


Fig. 6 All ^{14}C ages calibrated to years CE using OxCal (v.4.4.4) with the 95.4% confidence range (black o = median, black + = mean). First appearance of *Erodium* is shown with a red + and its approximate age range (Mensing et al. 1998).

Ambient versus event sedimentation as determined by PC1 values are shown along the left y-axis. Proposed maximum age of EU 1 and EU 2 are shown bolded text at the 95.4% confidence range

the 1760 CE SBB flood unit. The timing of these events within the LIA agrees with regional archives that suggest a wetter, stormier LIA hydroclimate.

However, without older sediments pre-dating the LIA at our site, we cannot say unequivocally that the LIA was wetter-than-average in the Carrizo Plains. This

study demonstrates that sag ponds represent a viable archive for capturing and preserving SPE flood units, especially in regions where natural lakes are rare—such as Southern California. Future work should follow a similar protocol as that used here—core transects along the sag pond's long axis, ^{14}C ages from ambient and event sediment, and varied sedimentological analyses.

Acknowledgements We acknowledge the indigenous lands of the Kuyam, Yokuts, Salinan, and Chumash where this research was conducted (native-land.ca). Thank you to the BLM for site access and assistance with the research request and site access.

Author contributions MEK, SH, and JC wrote the main manuscript text and MEK prepared all figures and tables. All authors reviewed the manuscript.

Funding This research was supported by the Southern California Earthquake Center (Contribution No. 13320). SCEC is funded by NSF Cooperative Agreement EAR-1600087 & USGS Cooperative Agreement G17AC00047. This project was also supported by Project RAISE, U.S. Department of Education HSI-STEM award number P031C160152.

Declarations

Conflict of interest We declare that the authors have no competing interests as defined by Springer, or other interests that might be perceived to influence the results and/or discussion reported in this paper.

References

- Akciz SO, Ludwig LG, Arrowsmith JR, Zielke O (2010) Century-long average time intervals between earthquake ruptures of the San Andreas fault in the Carrizo Plain, California. *Geology* 38:787–790
- Anderson RY (1977) Short-term sedimentation response in lakes in western United States as measured by automated sampling. *Limnol Oceanogr* 22:423–433
- Bailey HP (1966) The climate of Southern California. University of California Press, New York
- Bennett K, Willis K (2002) Pollen. In: Tracking environmental change using lake sediments, pp 5–32
- Bevis M, Hudnut K (2005) B4 lidar project: airborne laser swath mapping (ALSM) survey of the San Andreas Fault (SAF) system of central and southern California, including the Banning segment of the SAF and the San Jacinto fault system. National Center for Airborne Laser Mapping (NCALM), U.S. Geological Survey, the Ohio State University, and the Southern California Integrated GPS Project. Distributed by OpenTopography. <https://doi.org/10.5066/F7TQ5ZQ6>. Accessed: 2023-11-07
- Bird BW, Lei Y, Perello M, Polissar PJ, Yao T, Finney B, Bain D, Pompeani D, Thompson LG (2017) Late-Holocene Indian summer monsoon variability revealed from a 3300-year-long lake sediment record from Nir'pa Co, southeastern Tibet. *The Holocene* 27:541–552
- Blais JM, Kalff J (1995) The influence of lake morphometry on sediment focusing. *Limnol Oceanogr* 40:582–588
- Bowman D, Korjenkov A, Porat N (2004) Late-Pleistocene seismites from Lake Issyk-Kul, the Tien Shan range, Kyrgyzstan. *Sed Geol* 163:211–228
- Bronk Ramsey C (2021) OxCal v4. 4.4. Retrieved from <https://c14.arch.ox.ac.uk/oxcal.html>
- Brown S, Bierman P, Lini A, Davis PT, Southon J (2002) Reconstructing lake and drainage basin history using terrestrial sediment layers: analysis of cores from a post-glacial lake in New England, USA. *J Paleolimnol* 28:219–236
- Buck-Diaz J, Evens J (2011) Carrizo Plain National Monument vegetation classification and mapping project. California Native Plant Society, California
- Castello AF, Shelton ML (2004) Winter precipitation on the US Pacific coast and El Nino-Southern oscillation events. *Int J Climatol* 24:481–497
- Cayan DR, Dettinger MD, Diaz HF, Graham NE (1998) Decadal variability of precipitation over western North America. *J Clim* 11:3148–3166
- Cayan DR, Peterson DH (1989) The influence of North Pacific atmospheric circulation on streamflow in the west. In: Peterson DH (ed) Aspects of climate variability in the Pacific and the Western Americas. Geophysical Monograph Series, AGU, pp 375–397
- Chiang JC, Friedman AR (2012) Extratropical cooling, inter-hemispheric thermal gradients, and tropical climate change. *Annu Rev Earth Planet Sci* 40:383–412
- Clarke KR, Somerfield PJ, Gorley RN (2008) Testing of null hypotheses in exploratory community analyses: similarity profiles and biota-environment linkage. *J Exp Mar Biol Ecol* 366:56–69
- Corbosiero KL, Dickinson MJ, Bosart LF (2009) The contribution of eastern North Pacific tropical cyclones to the rainfall climatology of the southwest United States. *Mon Weather Rev* 137(8):2415–2435
- Corringham TW, Ralph FM, Gershunov A, Cayan DR, Talbot CA (2019) Atmospheric rivers drive flood damages in the western United States. *Sci Adv* 5:eaax4631
- Corringham TW, McCarthy J, Shulgina T, Gershunov A, Cayan DR, Ralph FM (2022) Climate change contributions to future atmospheric river flood damages in the western United States. *Sci Rep* 12:13747
- Covault JA, Romans BW, Fildani A, McGann M, Graham SA (2010) Rapid climatic signal propagation from source to sink in a southern California sediment-routing system. *J Geol* 118:247–259
- Cvijanovic I, Santer BD, Bonfils C, Lucas DD, Chiang JC, Zimmerman S (2017) Future loss of Arctic sea-ice cover could drive a substantial decrease in California's rainfall. *Nat Commun* 8:1–10
- Davis MB, Ford MS (1982) Sediment focusing in Mirror Lake, New Hampshire. *Limnol Oceanogr* 27:137–150
- Dean WE (1974) Determination of carbonate and organic matter in calcareous sedimentary rocks by loss on ignition: comparison with other methods. *J Sediment Petrol* 44:242–248

- Dearing J (1991) Lake sediment records of erosional processes, environmental history and palaeolimnology. Springer, Netherlands, pp 99–106
- Dearing J (1997) Sedimentary indicators of lake-level changes in the humid temperate zone: a critical review. *J Paleolimnol* 18:1–14
- Dettinger M (2011) Climate change, atmospheric rivers, and floods in California—a multimodel analysis of storm frequency and magnitude changes. *JAWRA J Am Water Resour Assoc* 47:514–523
- Dettinger MD, Ralph FM, Das T, Neiman PJ, Cayan DR (2011) Atmospheric rivers, floods and the water resources of California. *Water* 3:445–478
- Du X, Hendy I, Schimmelmänn A (2018) A 9000-year flood history for Southern California: a revised stratigraphy of varved sediments in Santa Barbara Basin. *Mar Geol* 397:29–42
- Du X, Hendy I, Hinnov L, Brown E, Zhu J, Poulsen CJ (2021) High-resolution interannual precipitation reconstruction of Southern California: implications for holocene ENSO evolution. *Earth Planet Sci Lett* 554:116670
- Ely LL (1997) Response of extreme floods in the southwestern United States to climatic variations in the late Holocene. *Geomorphology* 19:175–201
- Engstrom WN (1996) The California Storm of January 1862. *Quat Res* 46:141–148
- Enzel Y, Brown WJ, Anderson RY, McFadden LD, Wells SG (1992) Short-duration Holocene lakes in the Mojave River drainage basin, Southern California. *Quat Res* 38:60–73
- Fægri K, Kaland PE, Krzywinski K (1989) Textbook of pollen analysis, 4th edn. Wiley, New York
- Gershunov A, Shulgina T, Clemesha RE, Guirguis K, Pierce DW, Dettinger MD, Lavers DA, Cayan DR, Polade SD, Kalansky J (2019) Precipitation regime change in Western North America: the role of atmospheric rivers. *Sci Rep* 9:9944
- Grant Ludwig L, Akciz SO, Noriega GR, Zielke O, Arrow-smith JR (2010) Climate-modulated channel incision and rupture history of the San Andreas Fault in the Carrizo Plain. *Science* 327:1117–1119
- Gray AB, Pasternack GB, Watson EB, Warrick JA, Goñi MA (2015) The effect of El Niño Southern Oscillation cycles on the decadal scale suspended sediment behavior of a coastal dry-summer subtropical catchment. *Earth Surf Proc Land* 40:272–284
- Håkanson L, Jansson M (1983) Principles of lake sedimentology. Springer, Berlin
- Hanson RT, Dettinger MD, Newhouse MW (2006) Relations between climatic variability and hydrologic time series from four alluvial basins across the southwestern United States. *Hydrogeol J* 14:1122–1146
- Harris SM, Carvalho LMV (2017) Characteristics of southern California atmospheric rivers. In: Theoretical and applied climatology
- Haug GH, Huguén KA, Sigman DM, Peterson LC, Rohl U (2001) Southward migration of the intertropical convergence zone through the Holocene. *Science* 293:1304–1308
- Hendy IL, Dunn L, Schimmelmänn A, Pak D (2013) Resolving varve and radiocarbon chronology differences during the last 2000 years in the Santa Barbara Basin sedimentary record, California. *Quat Int* 310:155–168
- Hendy IL, Napier TJ, Schimmelmänn A (2015) From extreme rainfall to drought: 250 years of annually resolved sediment deposition in Santa Barbara Basin, California. *Quat Int* 387:3–12
- Hilton J (1985) A conceptual framework for predicting the occurrence of sediment focusing and sediment redistribution in Small Lakes. *Limnol Oceanogr* 30:1131–1143
- Hiner CA, Kirby ME, Bonuso N, Patterson WP, Palermo J, Silveira E (2016) Late Holocene hydroclimatic variability linked to Pacific forcing: evidence from Abbott Lake, coastal central California. *J Paleolimnol* 56:299–313
- Honke JS, Pigati JS, Wilson J, Bright J, Goldstein HL, Skipp GL, Reheis MC, Havens JC (2019) Late Quaternary paleohydrology of desert wetlands and pluvial lakes in the Soda Lake basin, central Mojave Desert, California (USA). *Quat Sci Rev* 216:89–106
- Huang X, Swain DL (2022) Climate change is increasing the risk of a California megaflood. *Sci Adv* 8:eabq0995
- Huang X, Swain DL, Hall AD (2020) Future precipitation increase from very high resolution ensemble downscaling of extreme atmospheric river storms in California. *Sci Adv* 6:eaba1323
- Kirby ME, Lund SP, Patterson WP, Anderson MA, Bird BW, Ivanovici L, Monarrez P, Nielsen S (2010) A Holocene record of Pacific Decadal Oscillation (PDO)-related hydrologic variability in Southern California (Lake Elsinore, CA). *J Paleolimnol* 44:819–839
- Kirby ME, Zimmerman SRH, Patterson WP, Rivera JJ (2012) A 9170-year record of decadal-to-multi-centennial scale pluvial episodes from the coastal Southwest United States: a role for atmospheric rivers? *Quat Sci Rev* 46:57–65
- Kirby ME, Feakins SJ, Hiner CA, Fantozzi J, Zimmerman SRH, Dingemans T, Mensing SA (2014) Tropical Pacific forcing of Late-Holocene hydrologic variability in the coastal southwest United States. *Quat Sci Rev* 102:27–38
- Kirby ME, Knell EJ, Anderson WT, Lachniet MS, Palermo J, Eeg H, Lucero R, Murrieta R, Arevalo A, Silveira E, Hiner CA (2015) Evidence for insolation and Pacific forcing of late glacial through Holocene climate in the Central Mojave Desert (Silver Lake, CA). *Quat Res* 84:174–186
- Kirby M, Heusser L, Scholz C, Ramezan R, Anderson M, Markle B, Rhodes E, Glover K, Fantozzi J, Hiner C (2018) A late Wisconsin (32–10k cal a BP) history of pluvials, droughts and vegetation in the Pacific south-west United States (Lake Elsinore, CA). *J Quat Sci* 33:238–254
- Kirby M, Patterson W, Ivanovici L, Sandquist D, Glover K (2021) Evidence for a large middle Holocene flood event in the Pacific southwestern United States (Lake Elsinore, California), From Saline to Freshwater: The Diversity of Western Lakes in Space and Time, Editors: Scott W. Starratt, Michael R. Rosen, GSA Special Paper 536:143–155
- Kirby M, Barbosa J, Carlin J, MacDonald G, Leidelmeijer J, Bonuso N, Han J, Nauman B, Avila J, Woodward A (2023) Holocene hydroclimatic variability recorded in sediments from Maddox Lake (northern California Coast Range). *Quat Res* 115:1–19
- Konrad CP, Dettinger MD (2017) Flood runoff in relation to water vapor transport by atmospheric rivers over the western United States, 1949–2015. *Geophys Res Lett* 44:11456–11462

- Koutavas A, Joanides S (2012) El Niño-Southern Oscillation extrema in the Holocene and Last Glacial Maximum. *Paleoceanography* 27:PA4208
- Lapointe F, Bradley RS (2021) Little Ice Age abruptly triggered by intrusion of Atlantic waters into the Nordic Seas. *Sci Adv* 7:eabi8230
- Leidemeijer JA, Kirby MEC, MacDonald G, Carlin JA, Avila J, Han J, Nauman B, Loyd S, Nichols K, Ramezan R (2021) Younger Dryas to early Holocene (12.9 to 8.1 ka) limnological and hydrological change at Barley Lake, California (northern California Coast Range). *Quat Res* 103:1–15
- Loisel J, MacDonald GM, Thomson MJ (2017) Little Ice Age climatic erraticism as an analogue for future enhanced hydroclimatic variability across the American Southwest. *PLoS ONE* 12:e0186282
- MacDonald GM, Kremenetski KV, Hidalgo HG (2008) Southern California and the perfect drought: Simultaneous prolonged drought in southern California and the Sacramento and Colorado River systems. *Quat Int* 188:11–23
- MacDonald GM, Moser KA, Bloom AM, Potito AP, Porinchu DF, Holmquist JR, Hughes J, Kremenetski KV (2016) Prolonged California aridity linked to climate warming and Pacific sea surface temperature. *Sci Rep* 6
- Masson-Delmotte V, Schulz M, Abe-Ouchi A, Beer J, Ganopolski A, Rouco JFG, Jansen E, Lambeck K, Luterbacher J, Naish T, Osborn T, Otto-Bliesner B, Quinn T, Ramesh R, Rojas M, Shao X, Timmermann A (2013) Information from Paleoclimate Archives. In: Stocker TF, Qin D, Plattner G-K, Tignor M, Allen SK, Boschung J, Nauels A, Xia Y, Bex V, Midgley PM (eds) *Climate change 2013: the physical science basis. Contribution of working group I to the fifth assessment report of the intergovernmental panel on climate change*. Cambridge University Press, Cambridge, New York
- Masters PM (2006) Holocene sand beaches of southern California: ENSO forcing and coastal processes on millennial scales. *Palaeogeogr Palaeoclimatol Palaeoecol* 232:73–95
- McPherson JG, Shanmugam G, Moiola RJ (1987) Fan-deltas and braid deltas: varieties of coarse-grained deltas. *Geol Soc Am Bull* 99(3):331–340
- Meko DM, Woodhouse CA, Bigio ER (2017) Southern California Tree-Ring Study. Final Report to California Department of Water Resources
- Mensing S, Byrne R (1998) Pre-mission invasion of *Erodium cicutarium* in California. *J Biogeogr* 25:757–762
- Migowski C, Agnon A, Bookman R, Negendank JF, Stein M (2004) Recurrence pattern of Holocene earthquakes along the Dead Sea transform revealed by varve-counting and radiocarbon dating of lacustrine sediments. *Earth Planet Sci Lett* 222:301–314
- Miller DM, Schmidt KM, Mahan SA, McGeehin JP, Owen LA, Barron JA, Lehmkühl F, Lohrer R (2010) Holocene landscape response to seasonality of storms in the Mojave Desert. *Quat Int* 215:45–61
- Montenat C, Barrier P, Hirsch C (2007) Seismites: An attempt at critical analysis and classification. *Sed Geol* 196:5–30
- Payne AE, Demory M-E, Leung LR, Ramos AM, Shields CA, Rutz JJ, Siler N, Villarini G, Hall A, Ralph FM (2020) Responses and impacts of atmospheric rivers to climate change. *Nat Rev Earth Environ* 1:143–157
- Polade SD, Gershunov A, Cayan DR, Dettinger MD, Pierce DW (2017) Precipitation in a warming world: assessing projected hydro-climate changes in California and other Mediterranean climate regions. *Sci Rep* 7:10783
- Porter K, Wein A, Alpers C, Baez A, Barnard P, Carter J, Corsi A, Costner J, Cox D, Das T, Dettinger M, Done J, Eadie C, Eymann M, Ferris J, Gunturi P, Hughes M, Jarrett R, Johnson L, Dam Le-Griffin H, Mitchell D, Morman S, Neiman P, Olsen A, Perry S, Plumlee G, Ralph M, Reynolds D, Rose A, Schaefer K, Serakos J, Siembieda W, Stock J, Strong D, Sue Wing I, Tang A, Thomas P, Topping K, Wills C, Jones L (2011) Overview of the ARKStorm scenario, U.S. Geological Survey Open-File Report, p 183
- Pribyl P, Shuman BN (2017) A computational approach to Quaternary lake-level reconstruction applied in the central Rocky Mountains, Wyoming, USA. *Quat Res* 82:249–259
- Ralph FM, Dettinger MD (2011) Storms, floods, and the science of atmospheric rivers. *EOS Trans Am Geophys Union* 92:265
- Reimer PJ, Austin WEN, Bard E, Bayliss A, Blackwell PG, Bronk Ramsey C, Butzin M, Cheng H, Edwards RL, Friedrich M, Grootes PM, Guilderson TP, Hajdas I, Heaton TJ, Hogg AG, Hughen KA, Kromer B, Manning SW, Muscheler R, Palmer JG, Pearson C, van der Plicht J, Reimer RW, Richards DA, Scott EM, Southon JR, Turney CSM, Wacker L, Adolphi F, Büntgen U, Capano M, Fahrni SM, Fogtmann-Schulz A, Friedrich R, Köhler P, Kudsk S, Miyake F, Olsen J, Reinig F, Sakamoto M, Sookdeo A, Talamo S (2020) The IntCal20 Northern hemisphere radiocarbon age calibration curve (0–55 cal kBP). *Radiocarbon* 62:725–757
- Reynolds LC, Simms AR, Ejarque A, King B, Anderson RS, Carlin JA, Bentz JM, Rockwell TK, Peters R (2018) Coastal flooding and the 1861–2 California storm season. *Mar Geol* 400:49–59
- Romans BW, Normark WR, McGann MM, Covault JA, Graham SA (2009) Coarse-grained sediment delivery and distribution in the Holocene Santa Monica Basin, California: implications for evaluating source-to-sink flux at millennial time scales. *Geol Soc Am Bull* 121:1394–1408
- Rustic GT, Koutavas A, Marchitto TM, Linsley BK (2015) Dynamical excitation of the tropical Pacific Ocean and ENSO variability by Little Ice Age cooling. *Science* 350:1537–1541
- Sabatier P, Moernaut J, Bertrand S, Van Daele M, Kremer K, Chaumillon E, Arnaud F (2022) A review of event deposits in lake sediments. *Quaternary* 5:34
- Sarno CT, Benitez-Nelson CR, Ziolkowski LA, Hendy IL, Davis CV, Tappa EJ, Thunell RC (2020) The impacts of flood, drought, and turbidites on organic carbon burial over the past 2,000 years in the Santa Barbara Basin, California. *Paleoceanogr Paleoclimatol* 35:e2020PA003849
- Schimmelmann A, Zhao M, Harvey CC, Lange CB (1998) A large California flood and correlative global climatic events 400 years ago. *Quat Res* 49:51–61
- Shuman BN, Serravezza M (2017) Patterns of hydroclimatic change in the Rocky Mountains and surrounding regions since the last glacial maximum. *Quat Sci Rev* 173:58–77

- Slawinska J, Robock A (2018) Impact of volcanic eruptions on decadal to centennial fluctuations of Arctic sea ice extent during the last millennium and on initiation of the Little Ice Age. *J Clim* 31:2145–2167
- Smith SG, Wegmann KW, Leithold EL, Bohnenstiehl DR (2019) A 4000-year record of hydrologic variability from the Olympic Mountains, Washington, USA. *The Holocene* 29:1273–1291
- Somerfield PJ, Clarke KR (2013) Inverse analysis in non-parametric multivariate analyses: distinguishing groups of associated species which covary coherently across samples. *J Exp Mar Biol Ecol* 449:261–273
- Stuiver M, Polach HA (1977) Discussion reporting of ^{14}C data. *Radiocarbon* 19:355–363
- Swain DL, Langenbrunner B, Neelin JD, Hall A (2018) Increasing precipitation volatility in twenty-first-century California. *Nat Clim Chang* 8:427–433
- Wentworth CK (1922) A scale of grade and class terms for clastic sediments. *J Geol* 30:377–392
- Wilhelm B, Arnaud F, Enters D, Allignol F, Legaz A, Magand O, Révillon S, Giguët-Covex C, Malet E (2012) Does global warming favour the occurrence of extreme floods in European Alps? First evidences from a NW Alps proglacial lake sediment record. *Clim Change* 113:563–581
- Wise EK (2010) Spatiotemporal variability of the precipitation dipole transition zone in the western United States. *Geophys Res Lett* 37:L07706
- Wise EK (2016) Five centuries of US West Coast drought: occurrence, spatial distribution, and associated atmospheric circulation patterns. *Geophys Res Lett* 43:4539–4546

Publisher's Note Springer Nature remains neutral with regard to jurisdictional claims in published maps and institutional affiliations.

Springer Nature or its licensor (e.g. a society or other partner) holds exclusive rights to this article under a publishing agreement with the author(s) or other rightsholder(s); author self-archiving of the accepted manuscript version of this article is solely governed by the terms of such publishing agreement and applicable law.